INVITED REVIEW PAPER

Key technological elements in dye-sensitized solar cells (DSC)

Shi-Woo Rhee[†] and Woosung Kwon

System on Chip Chemical Process Research Center, Department of Chemical Engineering,
Pohang University of Science and Technology (POSTECH), San 31, Hyoja-dong, Nam-gu, Pohang 790-784, Korea

(Received 24 May 2011 • accepted 6 June 2011)

Abstract−The best cell efficiency of lab scale dye sensitized solar cell (DSC) exceeds 11%, but there are still many technological problems to overcome for commercialization. This review describes key technological elements in DSC, including working electrodes with dye/TiO₂/electrolyte interfaces, quasi solid state electrolyte with ion diffusion, and counter electrodes with electrolyte-catalytic electrode interfaces. Their operating principles, equivalent electric circuits and measurement techniques are described.

Key words: Dye-sensitized Solar Cells, TiO₂-dye Junctions, Electrolytes, Counter Electrodes, Electrochemical Impedance Spectroscopy

INTRODUCTION

The conversion of solar radiation to electrical energy (photovoltaics) has become more and more important because sunlight is a clean and limitless energy source compared to the traditional fossil energy sources. Up to now, solid state junction devices based on crystalline silicon (so called the first generation solar cell with market share more than 80%) and thin films (second generation solar cell) based on amorphous silicon, CdTe (cadmium telluride), CIGS (copper-indium-gallium-selenide) and other compound semiconductors are dominant players in the market. For the crystalline silicon solar cell, high purity silicon (6-11N, i.e., impurity level in parts per million or billion range) is required in a form of a thin wafer (200 micron thick or lower) and a large amount of energy is required for purification and crystal growth. For the thin film solar cells, vacuum technique is required to deposit high purity films and it is not easy to integrate low cost and large scale production line.

Recently, the emergence of the third generation photovoltaic cells based on hybrid junctions (nanocrystalline inorganic materials and organic dye) and organic photovoltaic materials (polymers and low molecular weight organic compounds) has drawn much attention because they offer a possibility of low cost fabrication (solution based printing) together with other attractive features like flexibility. Despite its potential advantage, third generation solar cells still suffer from low conversion efficiencies and unproved long term stability and reliability. Among all the third generation solar cells, DSC based on mesoporous TiO₂/organometallic dye molecule junction appears to be most promising, and here some key technological aspects in the DSC are reviewed with a main focus on circuit elements, materials and interfaces. Readers are advised to refer to other review papers for more details [1-17].

CELL STRUCTURE AND OPERATION PRINCIPLES

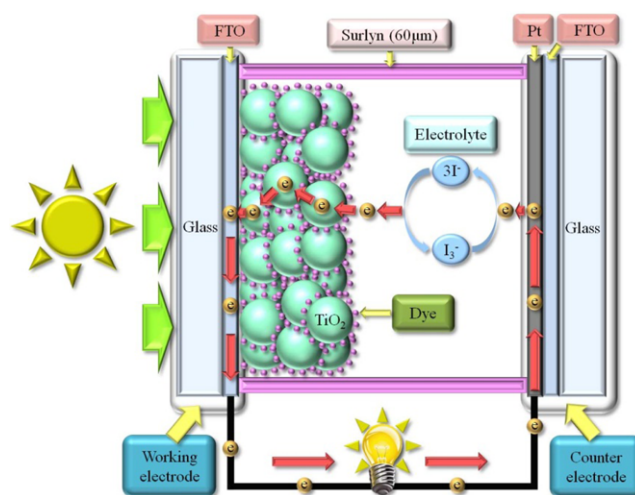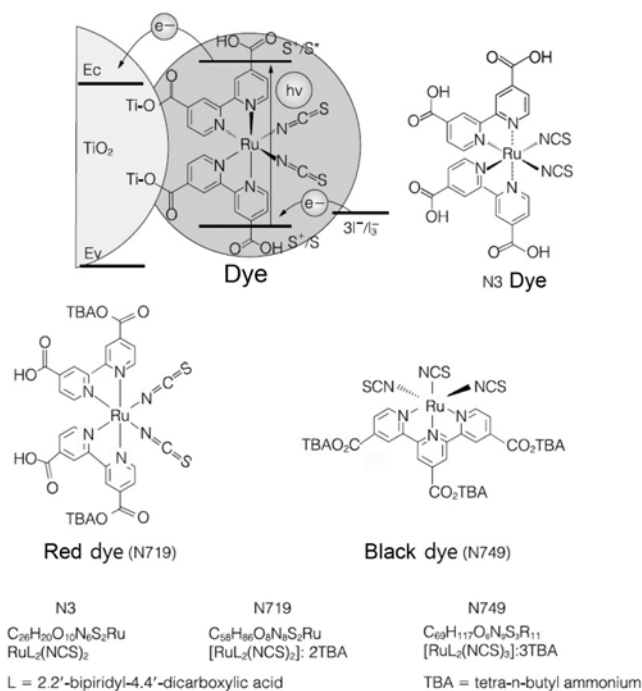The structure of the dye-sensitized solar cell is shown in Fig. 1.

[†]To whom correspondence should be addressed.
E-mail: srhee@postech.ac.kr

Fig. 1. Schematic diagram of the DSC with porous TiO₂/dye hybrid junction.

The solar radiation comes into the cell through the working electrode (PE: photoelectrode) made of a glass substrate with a transparent conduction oxide (TCO) film coated on it.

Currently, fluorine doped tin oxide (FTO: F-SnO₂) is widely used as a TCO material because it is stable at high temperature and has reasonable conductivity [18,19]. On top of the TCO layer, a porous layer of titanium oxide (10-15 μm thick) is formed by screen printing or doctor blading with 20 nm size titanium oxide paste, and the layer is sintered at 450-500 °C to increase the connectivity between particles and with the TCO layer. Then the working electrode is dipped in the organic dye solution and a monolayer of dye molecules (sensitizers) is formed on the titanium oxide surface through a chemisorption reaction. A redox electrolyte is in contact with the dye molecule and platinum (Pt) coated counter electrode (CE). When the light comes in, the cell starts to operate with the ultrafast injection of electrons from the photo-excited state of dye to the conduction band of the semiconductor. The counter electrode (CE) acts as an electron carrier from the external circuit to the redox electrolyte.

Fig. 2. Ruthenium based organometallic dyes widely used in the DSC.

The most widely used electrolyte system is the liquid phase I^-/I_3^- redox couple where iodide (I^-) ions reduce the oxidized dye, and the resultant triiodide (I_3^-) ions are reduced back to I^- at the CE [20]. Commonly, Pt is used as a catalyst for this reaction at the interface between the CE and the electrolyte.

Fig. 2 shows the molecular structure of three well known ruthenium based organometallic dyes used in DSC, so called N3, N719 and N749. Carboxyl group will react with Ti-OH on the titanium oxide surface for the chemisorption of the dye molecule and water molecule is released.

Like the chlorophyll involved in the natural process of photosynthesis in plants, when dye molecules absorb the incident solar light, electrons are excited from the highest occupied molecular level

Fig. 3. Potential energy structure of electrons and their transport in the DSC.

(HOMO) to the lowest unoccupied molecular level (LUMO). This is like a valence band (VB, E_v)-conduction band (CB, E_c) transition of electrons in silicon or other types of solar cells. Fig. 3 shows the potential energy structure and transport of electrons in DSC; the steps of the photoconversion process can be described in conjunction with the energy band diagram and the schematic structure of a DSC. The overall reactions involved in the cell are

$$TiO_2\text{-}S+h\nu \rightarrow TiO_2\text{-}S^* \tag{1}$$

$$TiO_2\text{-}S^* \rightarrow TiO_2\text{-}S^+ + e_{cb} \tag{2}$$

$$TiO_2\text{-}S^+ + e_{cb} \rightarrow TiO_2\text{-}S \tag{3}$$

$$TiO_2\text{-}S^+ + 3/2\ I^- \rightarrow TiO_2\text{-}S + 1/2\ I_3^- \tag{4}$$

$$1/2\ I_3^- + e_{Pt} \rightarrow 3/2\ I^- \tag{5}$$

$$I_3^- + 2e_{cb} \rightarrow 3\ I^- \tag{6}$$

Transitions occur in a time scale of milli, micro, nano and pico seconds. When light is absorbed, the dye (S) reaches an excited state (S*) and electrons are injected within femtoseconds into the conduction band of a large band gap semiconductor layer (E_g=3.2 eV for TiO$_2$) (1, 2). The electrons are transported through the TiO$_2$ layer by diffusion and reach the anode of the cell to be utilized in the external circuit. Some of the electrons will recombine with excited dye (3), which is the loss mechanism (II), and with I_3^- in the electrolyte (6), which is the loss mechanism (I) in Fig. 3. The suppression of these loss mechanisms is needed to enhance the cell efficiency. The oxidized dye (S$^+$) will be reduced back to the ground state (4) with the donation of an electron from I^- in the electrolyte (or the donation of a hole to the electrolyte). This leads to the regeneration of the charge neutral state of the sensitizer and the conversion of I^- to I_3^-. I_3^-, the carrier of the positive charge, will diffuse to the cathode (CE) while I^-, the carrier of the negative charge, will diffuse away from CE to anode (PE). On the Pt surface at CE, I_3^- receives electrons and is reduced back to I^- (5). This process requires a catalytic functionality of Pt on the cathode surface. This charge transfer rate is determined either by the electrochemical reaction on the catalyst surface or by the diffusion through the electrolyte. Overall, the photoconversion process is regenerative and there is no net change in the cell. The mesoporous TiO$_2$ layer provides enough surface area more than 1,000 times larger than that of a flat surface and allows the liquid electrolyte to fill all pores for efficient dye-ion contact. The charges are separated at the TiO$_2$/dye/electrolyte interface, and the extracted current is the sum of all active molecular charge generators connected in parallel. This allows effective initial charge separation because only the dye molecules absorb the light and generate the charge carriers, while charge transport occurs in the TiO$_2$ layer and the electrolyte. There is no minority carrier recombination, which allows a relatively high tolerance for impurities. Some electrons go down to the ground state in the dye molecule instead of moving to the TiO$_2$ conduction band, which is the loss mechanism (III) in Fig. 3.

A solar cell is a diode and in Fig. 4, a current-voltage (I-V) characteristic of a diode device is shown. At the reverse bias voltage (V<0) in dark state, there is no net current flow except a low level of leakage, but when the light illuminates the semiconductor surface, the characteristic curve shifts downward as shown in Fig. 4(a) and a solar cell I-V characteristics are usually represented as Fig.
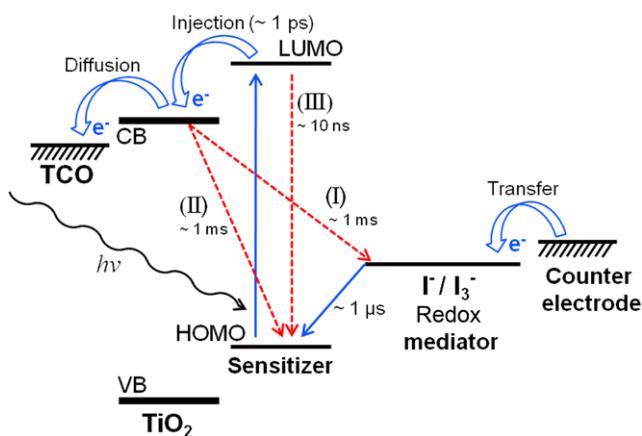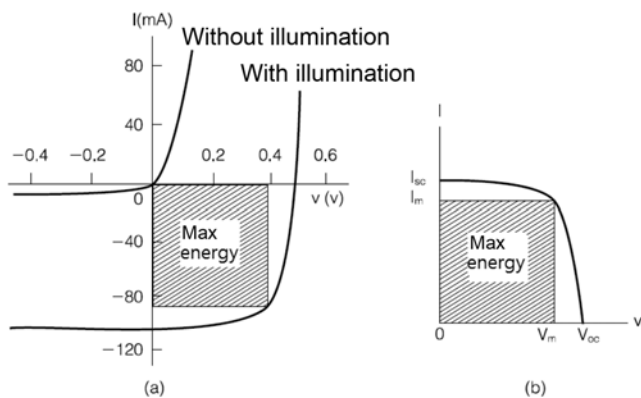
Fig. 4. (a) An I-V characteristic of a diode with or without solar illumination and (b) general representation of a solar cell I-V characteristics (V_{oc}: open circuit voltage, I_{sc}: closed circuit current).

4(b) without considering the sign of the current.

In a dark state without illumination, the I-V characteristic of a diode is given as

$$I = I_s \left[\exp\left(\frac{eV}{kT}\right) - 1 \right] \tag{7}$$

where I_s (dark current) is the saturation current under reverse bias (a leakage current due to the thermal excitation) and V is the applied voltage. When the light shines, a photocurrent is generated and the I-V characteristic equation becomes

$$I = I_s \left[\exp\left(\frac{eV}{kT}\right) - 1 \right] - I_p \tag{8}$$

where I_p is a photocurrent. Current density J is the current per unit area. Here I_{sc} is called the short circuit current, which is when there is no externally applied voltage and from Eq. (8),

$$I_{sc} = -I_p \tag{9}$$

V_{oc} is called the open circuit voltage, which is a voltage applied to make the current flow zero in the cell and from Eq. (8),

$$V_{oc} = \frac{kT}{e} \ln\left(1 + \frac{I_p}{I_s}\right) \tag{10}$$

With illumination, V_{oc} cannot be increased over an equilibrium value due to the recombination of the charge carriers; and in DSC, it is the difference between the conduction band of titanium oxide and the redox potential level of the electrolyte shown in Fig. 3. Maximum power (P_m) achievable from the cell is given from I_m and V_m in Fig. 4 as

$$P_m = I_m \times V_m \tag{11}$$

and the solar cell efficiency is

$$\eta = \frac{P_m}{P_{in}} \times 100\% \tag{12}$$

where P_{in} is the incoming solar energy. A fill factor, which shows how well we can utilize the incoming solar illumination, is defined as

$$FF = (I_m V_m)/(V_{oc} I_{sc}) \tag{13}$$

and it is around 0.7-0.8. DSC system is more complicated because electrochemical reactions and ion transport mechanisms are involved, but we can get similar I-V characteristic curves.

CIRCUIT DIAGRAMS AND ANALYSIS

DSC is an electrochemical device so that an electrical circuit model can be built just like any other solar cell. It is important to set up the right circuit model and optimize each circuit element for better cell efficiency. DSC is mainly made of three components: the porous TiO₂ layer, the electrolyte, and the counter electrode, as shown in Fig. 1. They form two spatially separated interfaces, the TiO₂/electrolyte and electrolyte/counter electrode. Homogeneous charge transport in the mediums and heterogeneous charge transfer (electrochemical reaction) at the interfaces are strongly coupled all together, from which the electrochemical behavior of DSC arises. In the aspect of charge transmission, those electrochemical components throughout the cell can be considered as a barrier which can be represented in terms of electrochemical impedance. We now introduce how impedances in DSCs can be constructed and measured.

At solid/electrolyte interfaces, an electrical double layer is formed from the ions attracted to the surface charge via chemical interactions or the Coulomb force. Charge carriers can be stored in the double layer and this charge accumulation is represented by a capacitor. Also, electrons moving through such heterogeneous interfaces may suffer from a resistance, called the charge transfer resistance. Each interface has its characteristic double layer capacitance and charge transfer resistance, in which magnitudes are largely influenced by interfacial properties such as materials and structures. One can intuitively understand that electrons near any interface can now behave in two different ways: accumulation in a double layer or transfer via an interface. The impedance at an interface in DSCs is often described by a parallel combination of a resistor and a capacitor, which correspond to the charge transfer resistance and the double layer capacitance, respectively. For the charge transport in a homogeneous medium, no charge accumulation occurs and the impedance becomes just a resistor in this case. In addition, ion diffusion through a bulk electrolyte has an impedance of both resistive and capacitive components, the Warburg impedance.

Impedance describes not only the relative amplitudes of the voltage and current but also the relative phases. Impedance is represented as a complex number with frequency dependence, and this is the most important point to distinguish them from ideal resistors. At very high frequencies, most portions of current flow through the capacitor and the influence of the resistor is small. As the frequency decreases, the capacitor begins open, and more portions of current flow through the resistor. Finally, at the zero frequency (DC), the capacitor is completely open, and the whole current should flow through the resistor. The value of the impedance is now the same as the resistance of the resistor.

Since each impedance has different frequency dependence, we can investigate the impedances buried in DSC by applying AC voltage of varying frequency with electrochemical impedance spectroscopy (EIS). EIS has been most widely used among several techniques [21-27]. The EIS measures a steady-state current response to applied AC voltage as a function of the frequency. The AC voltage should have small amplitude so that the response of a system can
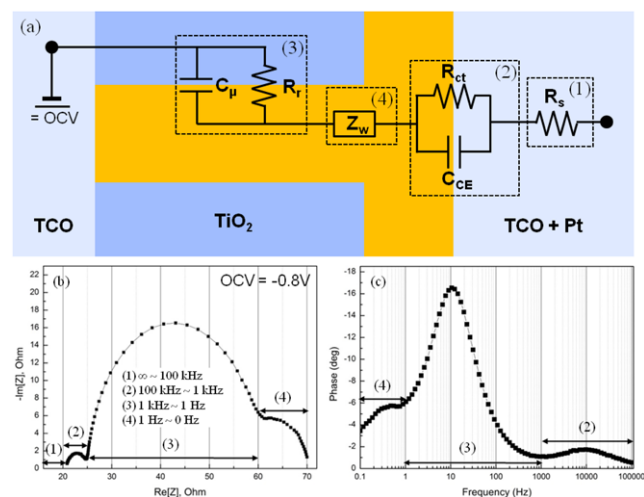
Fig. 5. (a) The equivalent circuit for DSC, (b) the Nyquist plot with characteristic semicircles and (c) the Bode plot with characteristic peaks.

be assumed to be pseudo-linear. Impedances at different parts of DSC may dominate at different frequencies as discussed earlier, and thus the frequency response obtained by the EIS can help decouple and identify the impedances in DSC.

To reveal underneath mechanisms buried in DSC using EIS, a proper equivalent circuit model should be arranged. One of the most widely accepted circuit models is shown in Fig. 5(a) with the circuit elements (1), (2), (3) and (4). The EIS data are expressed graphically in a Nyquist plot or a Bode plot. Impedance is a complex number and the Nyquist plot gives the imaginary part in y-axis and the real part in x-axis as a function of the frequency ω ($=2\pi f$), as shown in Fig. 5(b). On the other hand, the Bode plot in Fig. 5(c) shows the phase angle of the impedance in y-axis as a function of the log scale frequency on x-axis. Three semicircles in the Nyquist plot and three characteristic frequency peaks in the Bode represent the impedances in DSC. In the Nyquist plot at very high frequencies, current will flow through R_s and the capacitors in circuit elements (2), (3) and (4), and the value in the x-axis where the first circle begins in the left hand side corresponds to R_s. The resistance of the TCO on the left hand side and others are merged in R_s in this model. The high frequency semicircle ((2) in Fig. 5(b)) is assigned to the parallel combination of R_{ct} and C_{CE} at the electrolyte/counter electrode interface. Once the catalytic property of the counter electrode improves, R_{ct} decreases and the left-most semicircle becomes smaller. The intermediate frequency semicircle ((3) in Fig. 5(b)) is related to the recombination reaction and the charge accumulation at the TiO$_2$/electrolyte interface. Thus, the middle semicircle can be enlarged with the increase of R_r (retarding the recombination reaction). The last low frequency tail is attributed to the Warburg diffusion of the ions in the electrolyte.

When the frequency is very low down to zero, current will flow through the resistors in each circuit element and the value in the x-axis at the right end of the last semicircle will give the total resistance R_T ($=R_s+R_{ct}+R_w+R_r$) of the cell. On the other hand, in the Bode plot, the characteristic frequencies of a system can be easily determined by the peak positions along the x-axis. One important param-

eter obtained from the Bode plot is the electron lifetime in the TiO$_2$ layer, which can be estimated from the position of the mid-frequency peak ((3) in Fig. 5(c)) [28]. As the position of the peak moves toward the higher frequency regime, the electron lifetime becomes longer, that is, the recombination reaction is suppressed. One point to note is that a solar cell generates DC currents under solar radiation. In this case, the capacitive element in parallel with the resistive element will not play a role because all capacitors are open and current can flow only through the resistors. Thus, the situation of the cell in practical operation is quite apart from that of the EIS measurement.

So far, we briefly introduced the impedances in DSC and how they manifest themselves in the EIS measurement. Now, each impedance is considered part by part in more depth. Fig. 6 shows equivalent circuit models for the TiO$_2$/electrolyte interface. Since porous TiO$_2$ has a very small scale of a few tens of nanometers, charge carriers in transit are always adjacent to the surface, and thus the internal charge transport, charge accumulation, and heterogeneous charge transfer (recombination) are closely combined in a nontrivial manner. Bisquert et al. suggested that a thin porous semiconducting layer can be described theoretically by the transmission line model [29-32]. In the porous TiO$_2$ film, the internal charge transport occurs over a finite length and is coupled with the interfacial charge transfer resistance at each reaction site along the pores as shown in Fig. 6(a). Dye molecules attached on the TiO$_2$ surface are not directly influenced from the frequency modulation in the EIS, and thus are not represented as a distinct element in the circuit model [23]. Under illumination, however, they will place current sources at the TiO$_2$/electrolyte interface and affect severely the recombination rate of the cell [25]. In the case without illumination, the impedance of the transmission line model, Z, can be obtained as

$$Z=\left(\frac{R_t R_r}{1+i\omega/\omega_r}\right)^{1/2}\coth[(\omega_r/\omega_t)^{1/2}(1+i\omega/\omega_r)^{1/2}] \quad (14)$$

where R_t and R_r are the internal charge transport resistance and the recombination resistance, respectively. In the same manner, ω_t and ω_r are the corresponding characteristic frequencies. The lowercase letters in Fig. 6(a) denote the corresponding quantities per unit length and can be merged into the total quantities along a film of thickness L: R_t ($=r_t L$), R_r ($=r_r/L$), and C_μ ($=c_\mu L$). The double layer capacitance at the TiO$_2$/electrolyte interface is buried in $\omega_r=1/(R_r C_\mu)$. In the derivation of this equation, the diffusion impedance of iodide through the pores is neglected due to its high concentration and small size. For the DSC at the open-circuit condition, R_t can be neglected due to the highly conducting TiO$_2$ layer and in this case, R_r is much larger than R_t. Thus, when the frequency ω is much smaller than ω_r, Eq. (14) becomes

$$Z=\frac{1}{3}R_t+\frac{R_r}{1+i\omega/\omega_r} \; (R_r \gg R_t) \quad (15)$$

and the transmission line model is reduced into a simple model shown in Fig. 6(b). It should be noted that Eq. (15) is not valid for some cases. For instance, low-temperature sintered TiO$_2$ exhibits low conductivity due to a loose contact between neighboring particles, and R_t can be larger than R_r. In this case, Eq. (14) becomes the well-known Gerischer impedance [23].

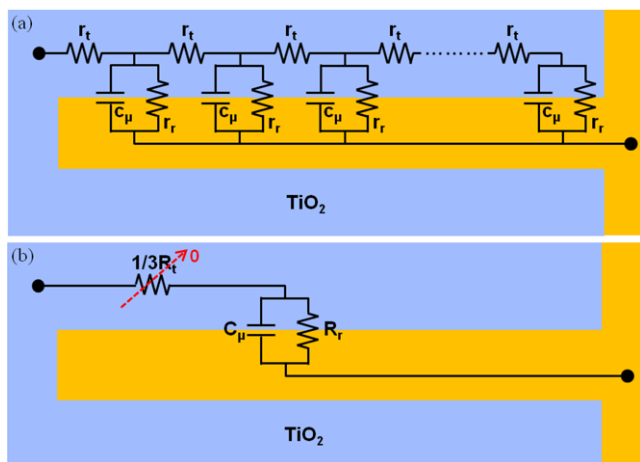The DSC includes the charge transport from the ion diffusion

Fig. 6. (a) The transmission line model for the porous TiO₂/electrolyte interface region and (b) the simplified circuit model for a conducting TiO₂ layer (when r_r can be neglected) which is part (3) in Fig. 5(a).

through the electrolyte. In practical I^-/I_3^- electrolyte, the concentration of triiodide is much lower than that of iodide, and furthermore, the diffusion rate of triiodide is slower than that of iodide due to the larger size of the I_3^- ion. Thus, the motion of triiodide mainly determines the diffusion impedance and the diffusion of triiodide within a finite length is well-described by the Warburg diffusion impedance Z_W according to the previous literatures [28,33]. From Fick's law with appropriate boundary conditions, the mathematical form of Z_W can be obtained as

$$Z_W = \frac{Z_0}{(i\omega)^{0.5}}\tanh(i\tau_d\omega)^{0.5} \qquad (16)$$

where ω is the angular frequency, Z_0 is the Warburg parameter, and τ_d is the characteristic diffusion time constant. The Nyquist plot of Z_W typically shows a straight line of slope 1 at higher frequencies

followed by a semicircle at lower frequencies.

At the electrolyte/counter electrode interface, the heterogeneous charge transfer, i.e., the reduction of triiodide to iodide, takes place with the help of catalysts. For electrodes with a macroscopically flat surface, the charge transfer impedance is assumed to be independent of the position and it can be described by one parallel combination of resistive and capacitive components. The respective components are defined as the charge transfer resistance, R_{ct} and the double layer capacitance at the counter electrode, C_{CE}. Thus, the overall impedance Z_{CE} can be expressed as [34]

$$Z_{CE} = \frac{R_{ct}}{1+i\omega C_{CE}R_{ct}} \qquad (17).$$

For electrodes with a thickness and pores, e.g., carbon electrodes, the Warburg diffusion impedance through the porous structure is combined in series with R_{ct} and the value of Z_{CE} should be altered [35-39].

TiO₂-DYE JUNCTION

In the DSC, dye molecules are chemisorbed on the TiO₂ porous layer surface to form TiO₂-dye junction, and visible light is absorbed by the sensitizer dye to generate excited electrons. This is the most important part in the DSC, just like the p-n junction in the silicon solar cell where photovoltaic conversion is enabled. There are many issues involved in that junction, but only core-shell structure and dye-coadsorbent parts will be described. Readers are advised to read other review papers for other issues. Electron injection from the excited state of the dye into the conduction band of the TiO₂ is followed by the subsequent regeneration of the dye by the I^-/I_3^- redox couple as shown in Eqs. (1)-(6). Efficient operation of the DSC device relies on the minimization of the possible recombination pathways occurring at the TiO₂/dye/electrolyte interface to allow the efficient charge transport through the TiO₂ porous layer and subsequent charge collection at the device contacts. The photo-generated electrons which

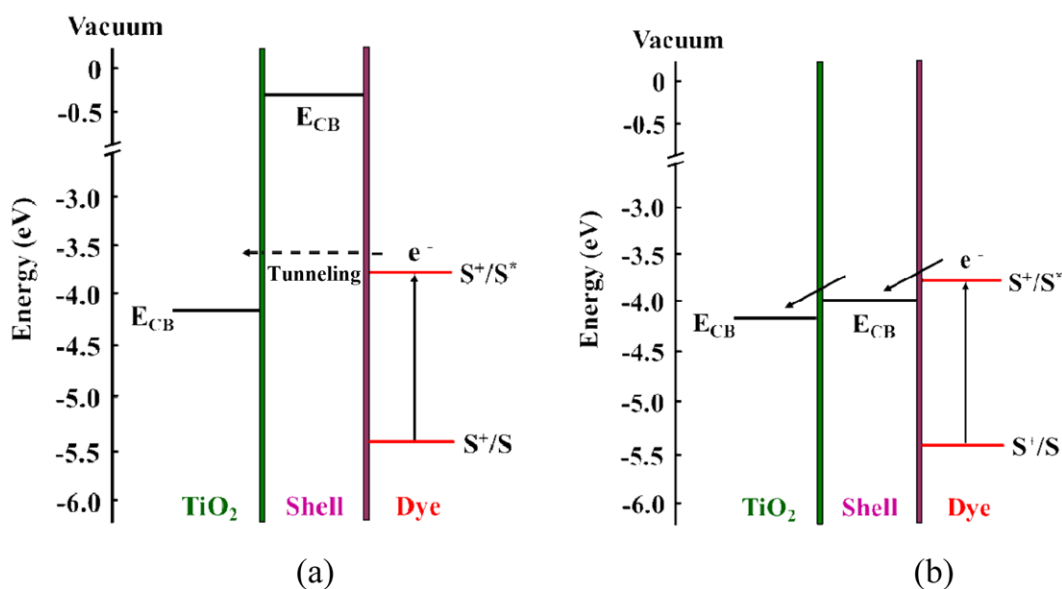Fig. 7. The potential energy structure of electrons with (a) insulating and (b) semiconducting shell materials on TiO₂. The energy level is given with the vacuum level as a reference (E=0).
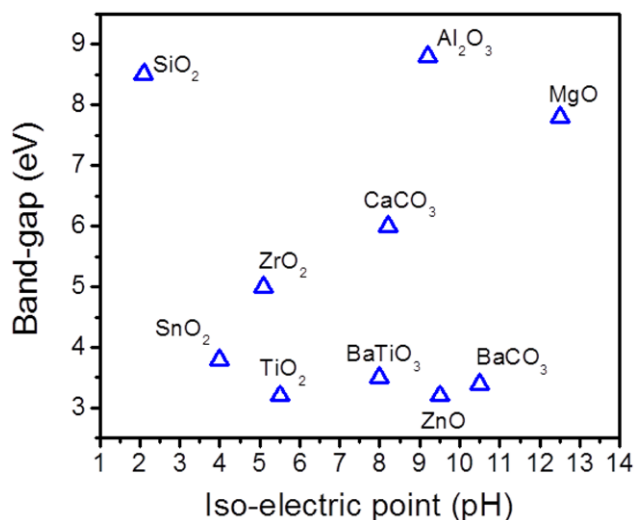
Fig. 8. The band gap and the iso-electric point of some oxide materials considered as a shell material in the DSC.

move to the TiO_2 conduction band may recombine either with oxidized dye molecules (process (II) in Fig. 3) or with the oxidized redox couple (process (I) in Fig. 3); the later reaction is thought to be particularly critical to the device performance.

To reduce the recombination, many groups have proposed device architectures [40-49], including the use of insulating polymers [42] and the use of very thin layered high band gap semiconductor metal oxides like ZnO and Nb_2O_5 [48-50]. Also, the use of insulating metal oxides like $CaCO_3$, $BaTiO_3$, MgO, and Al_2O_3 between the TiO_2 and dye interface has been tried [41,46,47,51-53]. Fig. 7 shows the two different cases of the energy band structure at the TiO_2-shell/dye interface. Fig. 7(a) is when the shell material has a high band gap and the energy barrier from the LUMO of the dye to the conduction band of the shell material is so high that the free electrons generated in the dye should tunnel through the layer to reach the conduction band of TiO_2. Fig. 7(b) is when the conduction band of the shell material is in between the LUMO of the dye and the conduction band of the TiO_2. In both cases, the back electron transport is suppressed to reduce the interfacial recombination, the loss mechanism in Fig. 3.

Fig. 8 shows the band gap and the iso-electric point of some oxide materials considered as a shell material in the DSC. High band gap materials (insulators) like SiO_2, MgO and Al_2O_3 will act as a barrier as shown in Fig. 7(a) and other materials with band gap slightly higher than TiO_2 will form an energy structure shown in Fig. 7(b). A material with high iso-electric point (more basic) will react more readily with carboxyl groups in the dye shown in Fig. 2. It was pointed out that a dipole in the shell layer formed on TiO_2 might shift the conduction band of the TiO_2, causing an increase in the open circuit voltage depending on the direction of the dipole. A practical application of core-shell structure was found to affect the solar cell performance in an uncertain and complicated way [40].

Al_2O_3 has been studied as an insulating barrier with its high conduction band edge compared to TiO_2. At the same time, high iso-electric point (IEP) of Al_2O_3 favors more dye adsorption for higher light absorption [47]. Kim et al. [54] proposed that open circuit voltage (V_{oc}) was closely related to the conduction band edge position
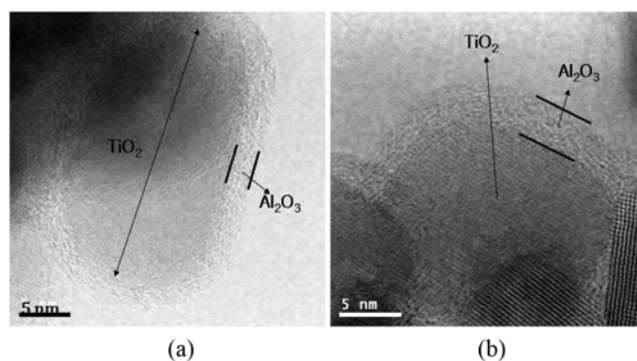
Fig. 9. High resolution transmission electron microscope (HR-TEM) images of TiO_2 porous layer covered with ALD alumina deposited with (a) 20 cycles and (b) 40 cycles [57].

and the band gap energy of the metal oxide shell layers, while the short circuit current density (J_{sc}) was related to the IEP. Most of the TiO_2 surface modifications using Al_2O_3 barrier layer were based on the simple solution deposition method and in this case, the precise control of the barrier thickness or conformal coating is not easy. Atomic layer deposition (ALD) is one alternative where precise control of the thickness and conformal coating is possible. ALD is an efficient way to control the nano structure and layer thickness by controlling the number of deposition cycles. A wide range of thicknesses for the Al_2O_3 barrier layer or shell layer from 0.1 to 12 nm have been reported for efficient DSCs [41,43,51-53,55,56].

It was revealed that there was an optimum thickness to reduce the recombination and at the same time to allow the electron flow from dye to TiO_2 layer without too much resistance [57]. To understand the effect of the barrier layer thickness on the device performance, Al_2O_3 shell/TiO_2 core structure was formed with ALD process and Fig. 9 shows the shell layer thickness as a function of the H_2O/TMA (trimethylaluminum) cycle. With 20 cycles, about 2 nm thick alumina layer was formed and 4 nm layer was obtained with 40 cycles. Fig. 10(a) shows the amount of dye adsorbed on the surface, and Fig. 10(b) shows the I-V characteristics of the cell both as a function of the alumina shell layer thickness. Cell parameters like open circuit voltage (V_{oc}) and closed circuit current (J_{sc}) along with the fill factor and efficiency are shown. To measure the amount of dye attached, KOH solution was used to dissolve out dyes from the surface after chemisorption and UV-visible absorption of the solution was measured.

Fig. 10(a) shows that the amount of dye adsorbed was increased as the shell layer thickness was increased. On the other hand, in Fig. 10(b), the I-V curve of the cell under AM 1.5 solar radiation (100 mW/cm^2) shows the maximum current level with the 2 nm thick shell. It shows about 35% improvement compared to bare TiO_2. As the thickness was increased, the efficiency was decreased even though the dye adsorption was increased due to the suppression of the tunneling through the shell layer.

Another method to improve the TiO_2-dye junction is to use the co-adsorbent. Modification of the interface by the introduction of co-adsorbents along with the dye can alter the conduction band edge and shield the trap states of TiO_2 to influence the V_{oc}, J_{sc}, and the recombination reaction of the photo-induced electrons [58-64]. It was reported that stearic acid as a co-adsorbent, which has a low

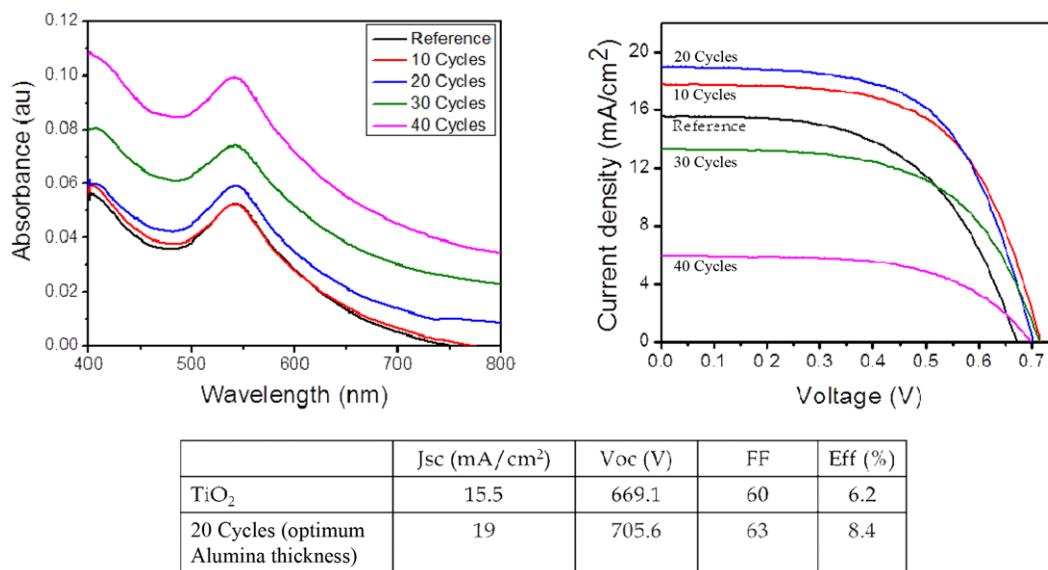|	Jsc (mA/cm²)	Voc (V)	FF	Eff (%)
TiO$_2$	15.5	669.1	60	6.2
20 Cycles (optimum Alumina thickness)	19	705.6	63	8.4

Fig. 10. (a) The amount of dye adsorbed on the surface and (b) the I-V characteristics of the cell as a function of the alumina shell layer thickness. Cell parameters like open circuit voltage, closed circuit current, fill factors and efficiency are given [57].

dipole moment and high solubility, hindered the rate of dye adsorption during the competitive anchoring process on the TiO$_2$ layer in DSC and increased the content of strongly bound dye on the TiO$_2$ surface [65]. This resulted in an approximately 25% improvement in J$_{sc}$ and the power conversion efficiency of the DSC even with much lower dye coverage.

In the formation of dye-TiO$_2$ junction, another problem is that it takes a long time for the chemisorption, and many research groups have studied to decrease the processing time [66-68]. DSC with the N719 dye required a dipping time of 12-24 h in a dye solution of 0.3-0.5 mM (1 mM=1×10^{-3} M), which is too long for commer-

Fig. 11. The schematic diagram of the drip and evaporation method.

cial production. Three methods were known in this regard and one method was to use the highly concentrated dye solution about 20 mM [69]. In this method, dye adsorption was finished in a few minutes but much of the expensive dye was unused and wasted. Another method was applying an electric field to the dye solution to enhance the negative dye ion movement towards the TiO$_2$ layer and the adsorption time was decreased down to 5 h at the concentration of 0.2 mM [68]. One can increase the temperature (80 $^\circ$C) of the dye solution and it could decrease the dye adsorption time down to 2 h at the concentration of 0.3 mM [70]. It was reported that the drip and evaporation method could reduce the dye adsorption time down to 1-4 min and the basic conceptual diagram is shown in Fig. 11 [71].

N719 dye was adsorbed on the TiO$_2$ surface through the reaction between the N719 dye and Ti-OH formed on TiO$_2$ nano-particle layer, and H$_2$O was generated from the reaction [72,73]. The N719 dye is non-volatile, but H$_2$O and solvent of the dye solution are volatile. The N719 dye solution contacts the surface of the 10 micron thick TiO$_2$ nano-particle layer with a 100 μm thick masking film at both ends. The glass substrate with the TiO$_2$ nano-particle layer on it is heated. The contact between the N719 dye molecule and the surface of the TiO$_2$ nano-particle increases with the solvent evaporation, and all the solvent is evaporated as time goes on. The dye molecules adsorb on the surface of the TiO$_2$ nano-particle and the adsorption rate is fast on the heated surface and, simultaneously, generated H$_2$O is also evaporated. The drip and evaporation method could decrease the dye adsorption time with the starting dye concentration below 0.3 mM without any loss of dye molecules and produce DSCs with efficiency slightly higher than the dipping method.

ELECTROLYTE

A redox electrolyte is an ionic solution containing a redox couple, and in DSCs the redox couple plays a central role. It regenerates the oxidized sensitizer and delivers the resulting holes to the
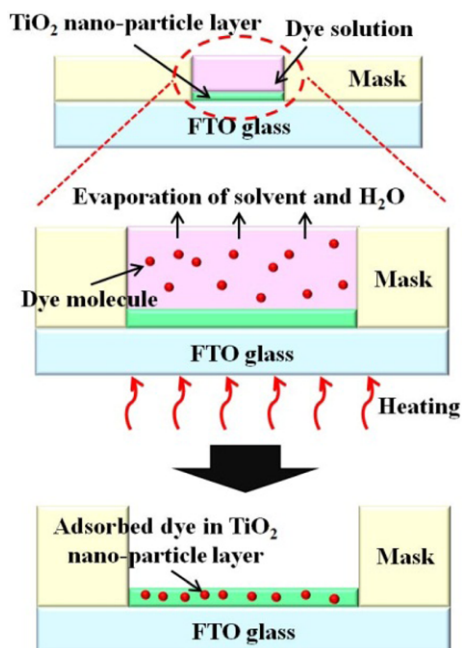
counter electrode to be reduced. The photovoltage is closely related to the redox couple because it sets the electrochemical potential at the counter electrode and affects the Fermi level of the photoelectrode via the recombination reaction [74-77] and the cation intercalation [78-80]. The photocurrent is also limited by the recombination reaction [81-84] and the diffusion of the redox couple [85,86].

The liquid phase iodide/triiodide redox couple has been the most widely used electrolyte in DSC due to its good solubility, low light-absorption, a suitable redox potential and rapid dye-regeneration. Above all, a very slow recombination reaction at the TiO$_2$/electrolyte interface is the main reason for the excellent performance of the iodide/triiodide redox couple. To prepare the iodide/triiodide-based electrolyte, some alkali metal iodides (LiI, NaI, KI, etc.) or imidazolium iodides (1-butyl-3-methylimidazolium iodide, etc.) with iodine are dissolved in a polar aprotic solvent such as acetonitrile. The ratio of iodide to iodine is typically 20 : 1 in liquid electrolyte-based DSCs. The iodide/triiodide-based liquid electrolyte enables a high efficiency of 11.5% in laboratory scale [87], but it shows several potential problems such as leakage of organic solvents, corrosion of metal electrodes and overpotential loss for the dye-regeneration.

The leakage issues (sealing) are strongly related to the long-term stability of DSCs. Solid-state and quasi-solid-state electrolytes such as polymer gel electrolytes [88-94], organic and inorganic hole transporting materials [95-101], ionic liquids [102-106], and polymer electrolytes [107-112] have been suggested in order to replace the conventional liquid electrolyte. Polymer gel electrolytes (PGEs) could reduce the leakage by retaining solvent molecules in the polymer matrices. Because of the gel characteristic, they exhibit high ionic conductivity comparable to the liquid electrolyte, reasonable permeability into the inner structure of the TiO$_2$ layer, and negligible vapor pressure. Polymers play a role of stiffener or plasticizer for solvents and DSCs with PGEs have attained high efficiencies of 8% in some cases. Since a three-dimensional network formed by polymers can interrupt the ion-diffusion, copolymers with low crystallinity exhibit relatively higher current density. Some derivatives of poly(vinylidene fluoride) (PVdF) and poly(ethylene oxide) (PEO) have been widely used in quasi-solid-state DSCs (qss-DSCs)

due to their good thermochemical and light-soaking stability. Interactions between polymer and solvent molecules should be also taken into account. Hydrophilic groups can help retain polar solvents by the van der Waals attraction and further facilitate dissolution of polymers. Meanwhile, unpaired electrons donated by oxygen or nitrogen groups stabilize cations in electrolytes due to the coulomb attraction. Polymer concentration of PGEs is another important factor largely affecting the cell performance. Here, we introduce an amphiphilic PGE (APGE) based on poly(lactic acid-co-glycolic acid) (PLGA) [113]. PLGA has been widely used to deliver biomedical drugs due to its good mechanical properties, low toxicity, and structural amorphousness [114]. A larger amount of polymer molecules provide more "cages" for solvent molecules to be retained so that long-term stability can be guaranteed. Also, concentration of the recombinative triiodide ions is lowered by polymer molecules, and thereby the recapture of photoelectrons is suppressed and the electron lifetime can be elongated. However, overuse of polymers may lower the ion diffusivity and limit the current density throughout the cell. Thus, certain compromise between stability and performance should be made in this case. Fig. 12(a) shows that the mass transfer control (plateau) of the Pt thin-layer symmetric cells intensifies, i.e., the mass transfer-limited current density decreases, as the PLGA concentration increases. Correspondingly, the Warburg diffusion impedance in Fig. 12(b) (the resistance of the arcs in the low frequency region) increases proportional to the PLGA concentration. Nevertheless the ion-diffusion becomes slower at higher polymer concentrations; DSCs with the 20 wt% and 40 wt% APGE in Fig. 13(a) have higher J_{sc} and comparable efficiencies (7.5 and 7.4%, respectively) to liquid electrolyte-based DSCs. Fig. 13(b) shows long-term stability of the APGE-based DSC. During 60 days for the APGE, the overall efficiency lies in ±5% of the initial value, whereas for the liquid electrolyte, the efficiency decreases by 30%.

Hole transporting materials (HTMs) are solid-state mediators which are absolutely free from leakage. In DSCs with HTMs, hole transfer takes place directly from the dye to the HTM and the holes are transported via electron hopping to a metal counter electrode. One of the most widely used HTMs is spiro-OMeTAD (2,2′,7,7′-tet-
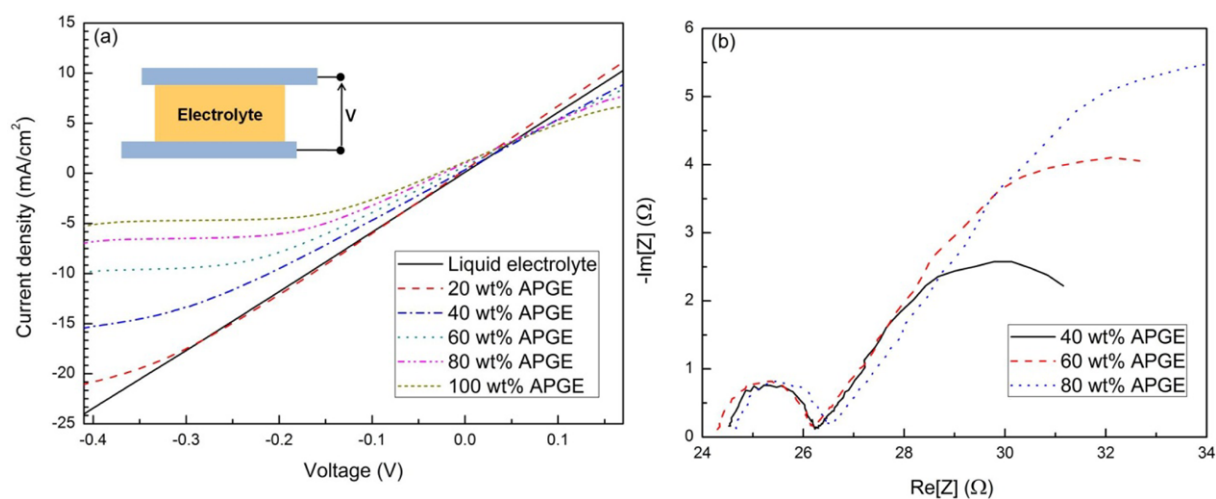
Fig. 12. Effect of the PLGA concentration on (a) the diffusive current plateaus and (b) the impedance spectra of the symmetric Pt thin-layer cells.
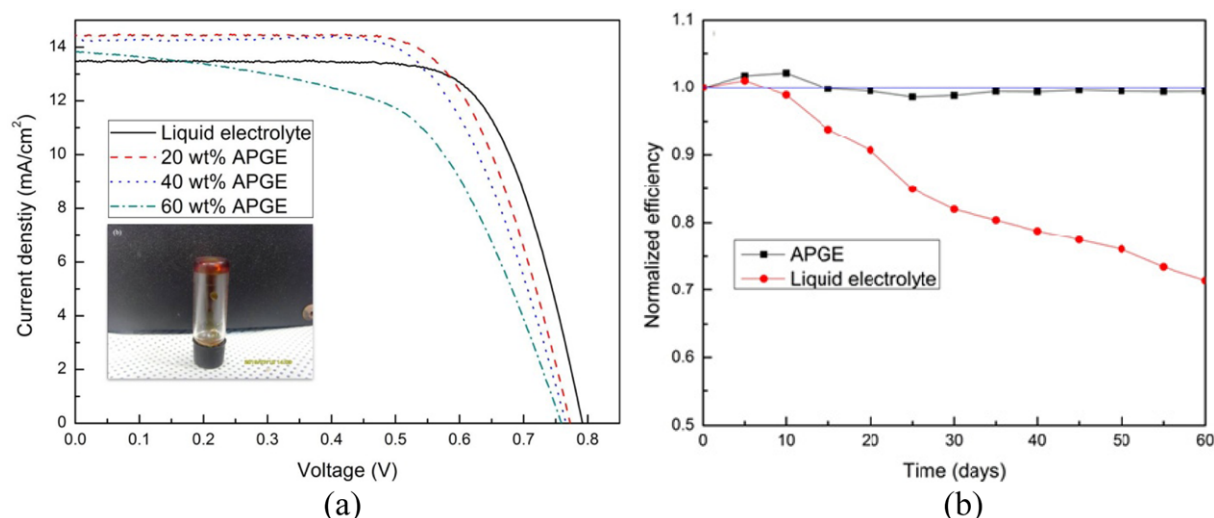
Fig. 13. (a) The current-voltage characteristics of the liquid electrolyte and APGE-based DSCs under irradiation of AM 1.5 simulated sunlight (100 mW cm^{-2}). The inset is a photograph of the 40 wt% APGE at 5 °C. (b) Normalized efficiencies for the DSCs with the liquid electrolyte and the 40 wt% APGE as a function of time.

rakis-(N,N-di-p-methoxyphenylamine)9,9′-spirobifluorene). Due to its small molecular size, high solubility, and amorphous nature, solid-state DSCs (ss-DSCs) with spiro-OMeTAD have attained efficiencies exceeding 5%, but they are still far below the efficiencies of liquid electrolyte DSCs. Such lower efficiencies can be mainly attributed to incomplete light harvesting. It is reported for ss-DSCs that the optimal thickness of the TiO$_2$ films is approximately 2 μm, which is much less than the optical depth for standard Ru-based sensitizers (ca. 10 μm for 90% absorption). The limitation to the film thickness may stem from the fast charge recombination and incomplete filling of the mesoporous films.

According to previous researches, the recombination in ss-DSCs is two orders of magnitude faster than that in liquid electrolyte DSCs and the electron diffusion length is limited to just a few micrometers [97,115,116]. However, Snaith et al. showed the electron diffusion length under short-circuit conditions is near 10 μm or longer [14]. In addition, a recent study introduced ion-coordinating Ru-based dyes, reducing the recombination rate, but the optimal thickness did not increase [117]. Thus, it is now concluded that infiltration of mesoporous TiO$_2$ with the HTM is crucial for enabling more efficient ss-DSCs with thicker films. Although mechanism of the infiltration was quantified and well established [118,119], and no breakthrough has been attained to date yet.

An ionic liquid is a salt in the liquid state that can be used as a solvent-free electrolyte. Ionic liquid-based DSCs have attained efficiencies over 7% with some low viscosity melts such as 1-ethyl-3-methylimidazolium thiocyanate [103], selenocyanate [105], tricyanomethide [120], and tetracyanoborate [121]. However, most of the low viscosity melts proved to be unstable under long-term thermal stress and light-soaking. Of the iodide melts, 1-propyl-3-methylimidazolium iodide (PMII) has the lowest viscosity and therefore shows so far the highest efficiency in solvent-free DSCs. Low viscosity of ionic liquids can facilitate the ion-diffusion and prevent loss of the fill factor during the cell operation. The viscosity of the iodide melts decreases as the length of the alkyl chain on imidazole decreases. Thus, it is expected that 1-ethyl-3-methylimidazo-

lium iodide (EMII) and 1,3-dimethylimidazolium iodide (DMII) can show higher conductivity than PMII. Unfortunately, they cannot form liquid at ambient temperature due to their conformational rigidity. Also, 1-allyl-3-methylimidazolium iodide (AMII) shows a higher conductivity than PMII above its melting point of 60 °C. In this manner, a ternary melt of DMII, EMII, and AMII has been suggested by Bai et al. to provide a room temperature ionic liquid with superior conductivity [106]. The resulting melt has a melting point below 0 °C due to the increase in entropy and shows the highest conductivity exceeding PMII. Solvent-free DSCs using the ternary melt with the Z907Na sensitizer show an unprecedented efficiency of 8.2% and prolonged stability under 1 Sun illumination.

Polymer electrolytes (PEs) are solid-state ionic conductors prepared by dissolving salts in polymers with polyether units. Ionic conductivity of PEs is closely related to the degree of crystallinity. For instance, PEO has a low glass transition temperature of −50 °C, but a high degree of crystallinity of 80% due to its structural regularity. Thus, PEO-based PEs exhibit very low conductivities in the order of 10^{-6} S/cm. To reduce crystallinity of polymers, a certain degree of irregularity should be introduced. This can be achieved by polymer blends, copolymers, cross-linking, or third-party inorganic particles. PEs incorporating inorganic nanoparticles, so called nanofillers, proved to be promising with high efficiencies of 4%. Stergiopoulos et al. reported that PEO of MW 2,000,000 mixed with TiO$_2$ nanoparticles ca. 25 nm has considerably lower crystallinity, and thereby higher conductivity is attained [109]. The polymer chains disordered by the TiO$_2$ fillers may provide apertures or "voids" through which the iodide/triiodide ions can migrate easily. DSCs with the PEO/TiO$_2$ composite electrolyte show high efficiencies of 4.2%. Many other inorganic nanoparticles such as ZnO, Al$_2$O$_3$, and SiO$_2$ have been also used as a filler in PEs, giving reasonable performance [122-125]. Recently, an attempt using a clay as a filler has been tried in PEs [126]. In this study, DSCs with a composite of PEO and clay-like montmorillonite show high mechanical robustness but low efficiencies of 3.2% at 10 mW cm^{-2} due to the incomplete infiltration of the electrolyte into mesoporous TiO$_2$ films.

The iodide/triiodide redox couple is highly corrosive, which can attack most metals. Platinum has proved to be one of the most effective catalysts in the DSC. However, it is reported that vapor-deposited platinum is dissolved out in the electrolyte containing the iodide/triiodide redox couple [127]. On the other hand, platinum deposited with thermal decomposition shows prolonged stability and is widely adopted in practical applications. For large-scale DSC modules, current-correcting metal grid made of silver or copper is generally patterned on the TCO side to reduce the series resistance. In this case, the metal grid is exposed to somewhat corrosive environment, so long-term stability might be a problem. Thus, several corrosion-free redox couples such as 2,2,6,6-tetramethyl-1-piperidinyloxy (TEMPO) [128] and disulfide/thiolate [129] have been suggested with some success. They are completely non-toxic organic mediators, but they show questionable stability under illumination and low cell performance. Metal coordination complexes using cobalt or copper can be another solution for corrosion. The HTMs and PEs introduced in the previous section can resolve the corrosion problems.

The redox potential of the iodide/triiodide couple is 0.35 V (vs. NHE: normal hydrogen electrode), and the oxidation potential of N719, the most widely used Ru-based sensitizer, is 1.1 V. Here, the overpotential driving the dye-regeneration is as large as 0.75 V. It should be noted that the dye regeneration is one-electron process. Since the oxidation of iodide to triiodide involves the transfer of two electrons, such a large driving potential is necessary to provide an intermediate step from iodide to iodine ion radical, I_2 [45]. If a half of this overpotential loss is gained without sacrificing the rapid dye-regeneration, efficiencies above 15% can be attained. One electron transfer redox couples such as $(SCN)_2/SCN$ and $(SeCN)_2/SeCN$ have been suggested earlier [130]. Although their redox potentials are much lower than the iodide/triiodide system, no improvement in open-circuit voltage was observed. This can be attributed to slow dye regeneration. Recently, several one-electron redox couples such as cobalt(II/III) [131] and copper(I/II) [132] complexes have been applied for straightforward dye regeneration processes. Their kinetic behavior can rival the iodide/triiodide redox couple. In particular, cobalt(II/III) has a weak visible light absorption, which indicates a feasibility of highly concentrated redox melts. However, performance in practical application is still limited by low solubility and slow diffusion of the mediators.

COUNTER ELECTRODE (CE)

The role of the counter electrode is to transfer electrons arriving from the external circuit back to the electrolyte and platinum (Pt) is a very effective catalyst to provide electrons into the electrolyte containing iodide (I^-) / triiodide (I_3^-) redox couple as shown in Eq. (5). The charge transfer resistance, R_{ct} at the electrolyte/counter electrode interface is an important parameter for the performance of DSCs [133-135], and it depends on the electrochemical reaction rate at the interface. To reduce R_{ct}, a material with high catalytic activity and high surface area should be used. In general, Pt is deposited on FTO glass to catalyze the reduction of the I_3^- ions and so far, several methods have been used such as thermal decomposition [135-138], sputtering [139,140], chemical deposition [141] and electrochemical deposition [142-144]. Thermal decomposition is com-

monly used to deposit Pt on FTO glass with wet process using Pt precursor solution (hexachloroplatinic acid, H_2PtCl_6). When a drop of the precursor solution is applied on FTO glass and annealed at 380-450 °C for 10-15 min, a Pt layer composed of nanoparticles are formed with a size about 6-10 nm and a thickness of a few nanometers. This layer shows excellent catalytic activity with low Pt loading (5-10 $\mu g/cm^2$) and low R_{ct} (0.07 $\Omega \cdot cm^2$) [135,138]. In addition, Pt layer deposited with thermal decomposition shows better stability and higher exchange current for I^-/I_3^- redox couple in the electrolyte than electrochemical deposition [135].

Sputtering is also used to deposit Pt onto the FTO glass and it shows high reproducibility, good adhesion to the substrate and the possibility of low temperature process [145]. It was shown with sputtering process that 2 nm thick Pt layer is effective enough for good catalytic activity [140]. Especially, sputtering is suitable for the fabrication of flexible DSC due to the low processing temperature but vacuum deposition method is not cost effective compared to the wet process. For flexible DSC, sputtered Pt on stainless steel or nickel sheet or ITO (indium tin oxide) on PEN (poly(ethylene naphthalenedicarboxylate)) sheet were tried [146]. Although FTO glass is widely used as a counter electrode substrate, it has problems such as high cost, fragility and shape limitation [147-150]. In addition, the performance of DSC based on large-scale FTO glass is poor because of the high sheet resistance [151,152]. Compared with TCO coated polymer films, low cost thin metallic foils are preferred because of the high conductivity, reflectance and flexibility [153,154]. High conductivity of thin metallic foils can reduce the internal resistance, leading to the increase in fill factor (FF) and conversion efficiency in DSC [155]. Especially, stainless steel (SUS) is a strong candidate material as a flexible counter electrode because it shows a high stability in the electrolyte containing I^-/I_3^- redox couple without any signs of corrosions [153,156,157]. Chen et al. fabricated DSCs with SUS and Ni sheet and Pt layer was deposited with wet chemical deposition using different concentrations of Pt precursor. Fang et al. [146] and Ma et al. [156] compared various flexible materials.

To study the counter electrode system with electrolytes, we do not have to make a full cell shown in Fig. 1 but can make a simple symmetric cell shown in Fig. 14. In this case, the circuit diagram will be (1)-(2)-(4)-(2)-(1) and each circuit element is shown in Fig. 5. From the EIS spectrum, we can get the charge transfer resistance at the interface of electrolyte/CE and diffusive resistance of the electrolyte. I-V characteristics and EIS spectrum in Fig. 12 were obtained with this symmetric cell.

Despite the advantage of platinum CE in DSC, higher cost, poor stability in corrosive electrolyte and high temperature processing
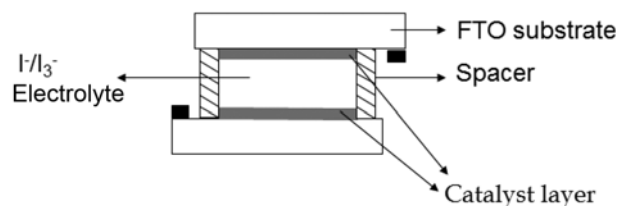

Fig. 14. Structure of a symmetric cell to study the charge transfer in the electrolyte/CE system.

drives the need for the development of alternative CE materials. In the recent past, a few groups reported on different CE materials like carbon nanotubes (CNT) [158,159], activated carbon, graphite [160], nanocarbon [161], mesoporous carbon [162,163] and conducting polymers [164,165]. For higher catalytic activity, some groups have reported carbon black and carbon black mixed with graphite as an efficient CE [166]. Carbon material has been used as an electrode material in an electrochemical device for a long time because it is stable, cheap, reasonably conductive and catalytic. There are various forms of carbon and some can be dispersed in a solvent to be used in a wet printing process such as doctor blading [167,168], screen printing [169], and spray coating [170].

In general, graphitic materials such as graphite and CNT are composed of basal and edge planes. Edge planes exhibit faster electron transport than basal planes, so edge planes act as the catalytic sites for the reduction of the I_3^- ions [171]. To improve the catalytic activity, carbon material should have high surface area with a number of the catalytic sites. Many groups have been extensively researching various parameters to increase the surface area, such as thickness [167,170,172,173], particle size [170,174] porosity [175] and orientation [176,177] of carbon materials. The catalytic electrode layer with carbon material is porous with a thickness of a few microns, and in this case, I_3^- ions should penetrate into the inner structure of the electrode to be reduced, and an additional diffusion impedance along the pores should be considered. Fig. 15(a) shows an equivalent circuit for the symmetric cell including ion diffusion through a porous electrode, $Z_{w,pore}$. Since Pt CE has a dense film structure, catalytic reaction may occur at the surface of the Pt layer; thus $Z_{w,pore}$ can be neglected as shown in (1)-(2)-(4) of Fig. 5(a).

In Fig. 15(b), the EIS spectra of two different symmetric cells using Pt or MWNT (multiwall carbon nanotube)/poly(3,4-ethylenedioxythiophene) polymerized with poly(4-styrenesulfonate) (PEDOT : PSS) composite as a catalytic layer are shown [177,178]. In symmetric cells, the high frequency (left) and the low frequency semicircle (right) are related to R_{ct} and Z_w, respectively. For the Pt symmetric cell, each semicircle has a clear appearance so that R_{ct} and Z_w can be decoupled completely. Thus, we can obtain exact value of the resistive component of each impedance. On the other hand, for the MWNT/PEDOT : PSS cell, the spectrum is rather indistinct due to $Z_{w,pore}$ in series with R_{ct}. In this case, it is difficult to decouple and extract any value of the resistive component, and only the total

resistance of the cell can be meaningful. The larger high frequency semicircle for MWNT/PEDOT : PSS can be attributed to the relatively poor catalytic activity of MWNT. Also, the low frequency tail may be intensified by $Z_{w,pore}$. The total resistance of the MWNT/PEDOT : PSS symmetric cell is higher than the Pt cell due to higher R_{ct} and additional $Z_{w,pore}$ and the cell performance will be poorer. More effort is in progress to optimize the carbon electrode for better DSC performance.

CONCLUSION

DSC is a front runner among all the third generation solar cells due to its high efficiency and low cost. There are still many hurdles to overcome for commercialization, and in this review, key technological elements were reviewed along with the basic principles to understand the DCS operations.

REFERENCES

1. M. Grätzel, *Nature*, **414**, 338 (2001).
2. M. Grätzel, *J. Photochem. Photobiol. C.*, **4**, 145 (2003).
3. D. F. Watson and G. J. Meyer, *Annu. Rev. Phys. Chem.*, **56**, 119 (2005).
4. B. A. Gregg, *Coord. Chem. Rev.*, **248**, 1215 (2004).
5. J. R. Durrant, S. A. Haque and E. Palomares, *Coord. Chem. Rev.*, **248**, 1247 (2004).
6. Z.-S. Wang, H. Kawauchi, T. Kashima and H. Arakawa, *Coord. Chem. Rev.*, **248**, 1381 (2004).
7. B. Li, L. Wang, B. Kang, P. Wang and Y. Qiu, *Sol. Energy Mater. Sol. Cells*, **90**, 549 (2006).
8. C. S. Karthikeyan and M. Thelakkat, *Inorg. Chim. Acta*, **361**, 635 (2008).
9. T. N. Murakami and M. Grätzel, *Inorg. Chim. Acta*, **361**, 572 (2008).
10. X. Chen and S. S. Mao, *Chem. Rev.*, **107**, 2891 (2007).
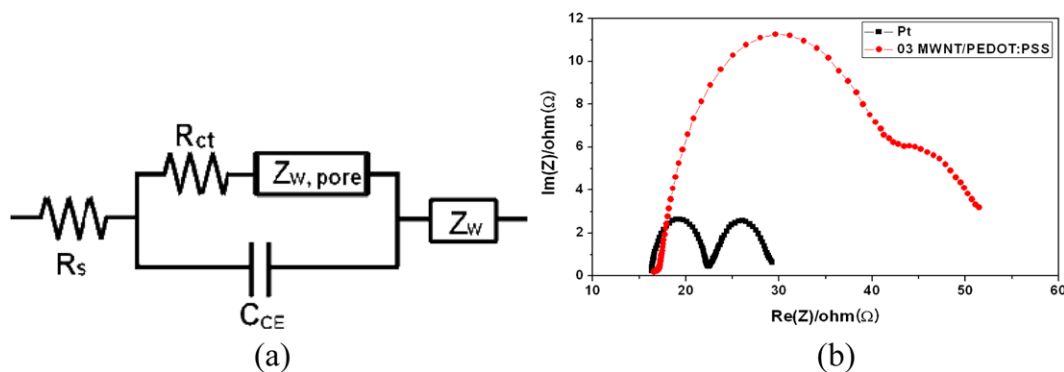11. A. Hagfeldt and M. Grätzel, *Acc. Chem. Res.*, **33**, 269 (2000).

Fig. 15. (a) An equivalent circuit diagram for a counter electrode system with pores and (b) an example of EIS spectrum for a symmetric cell with Pt or multiwall CNT/PEDOT:PSS composite electrode.

12. Q. Wang, S. M. Zakeeruddin, Md. K. Nazeeruddin, R. Humphry-Baker and M. Grätzel, *J. Am. Chem. Soc.*, **128**, 4446 (2006).

13. S. Güunes and N. S. Sariciftci, *Inorg. Chim. Acta*, **361**, 581 (2008).

14. H. J. Snaith and L. Schmidt-Mende, *Adv. Mater.*, **19**, 3187 (2007).

15. M. Grätzel, *Inorg. Chem.*, **44**, 6841 (2005).

16. J. Bisquert, D. Cahen, G. Hodes, S. Rhle and A. Zaban, *J. Phys. Chem. B*, **108**(24), 8106 (2004).

17. S. K. Deb, *Sol. Energy Mater. Sol. Cells*, **88**, 1 (2005).

18. C. G. Granqvist, *Sol. Energy Mater. Sol. Cells*, **91**, 1529 (2007).

19. R. G. Gordon, *MRS Bulletin*, **25**(8), 52 (2000).

20. B. A. Gregg, *J. Phys. Chem. B*, **107**, 4688 (2003).

21. F. Fabregat-Santiago, G. Garcia-Belmonte, J. Bisquert, A. Zaban and P. Salvador, *J. Phys. Chem. B*, **106**, 334 (2002).

22. A. Pitarch, G. Garcia-Belmonte, I. Mora-Sero and J. Bisquert, *Phys. Chem. Chem. Phys.*, **6**, 2983 (2004).

23. F. Fabregat-Santiago, J. Bisquert, G. Garcia-Belmonte, G. Boschloo and A. Hagfeldt, *Sol. Energy Mater. Sol. Cells*, **87**, 117 (2005).

24. J. Nelson, *Phys. Rev. B*, **59**, 15374 (1999).

25. Q. Wang, J.-E. Moser and M. Grätzel, *J. Phys. Chem. B*, **109**, 14945 (2005).

26. J. Bisquert, F. Fabregat-Santiago, I. Mora-Sero, G. Garcia-Belmonte and S. Gimenez, *J. Phys. Chem. C*, **113**, 17278 (2009).

27. M. Adachi, M. Sakamoto, J. Jiu, Y, Ogata and S. Isoda, *J. Phys. Chem. B*, **110**, 13872 (2006).

28. R. Kern, R. Sastrawan, J. Ferber, R. Stangl and J. Luther, *Electrochim. Acta*, **47**, 4213 (2002).

29. J. Bisquert, G. Garcia-Belmonte, F. Fabregat-Santiago, N. S. Ferriols, P. Bogdanoff and E. C. Pereira, *J. Phys. Chem. B*, **104**, 2287 (2000).

30. J. Bisquert, G. Garcia-Belmonte, F. Fabregat-Santiago, N. S. Ferriols, M. Yamashita and E. C. Pereira, *Electrochem. Commun.*, **2**, 601 (2000).

31. J. Bisquert, *Phys. Chem. Chem. Phys.*, **2**, 4185 (2000).

32. J. Bisquert, *J. Phys. Chem. B*, **106**, 325 (2002).

33. A. Hauch and A. Georg, *Electrochim. Acta*, **46**, 3457 (2001).

34. A. J. Bard and L. R. Faulkner, *Electrochemical methods: Fundamentals and applications*, 2nd Ed., John Wiley & Sons, New York (2000).

35. J. D. Roy-Mayhew, D. J. Bozym, C. Punckt and I. A. Aksay, *ACS Nano*, **4**, 6203 (2010).

36. W. J. Lee, E. Ramasamy, D. Y. Lee and J. S. Song, *Sol. Energy Mater. Sol. Cells*, **92**, 814 (2008).

37. B. Fang, S.-Q. Fan, J. H. Kim, M.-S. Kim, M. Kim, N. K. Chaudhari, J. Ko and J.-S. Yu, *Langmuir*, **26**, 11238 (2010).

38. G. Wang, W. Xing and S. Zhuo, *J. Power Sources*, **194**, 568 (2009).

39. S. Peng, F.Cheng, J. Shi, J. Liang, Z. Tao and J. Chen, *Solid state Sci.*, **11**, 2051 (2009).

40. Q. Zhang and G. Cao, *Nano Today*, **6**, 91 (2011).

41. E. Palomares, J. N. Clifford, S. A. Haque, T. Lutz and J. R. Durrant, *Chem. Commun.*, 1464 (2002).

42. B. A. Gregg, F. Pichot, S. Ferrere and C. L. Fields, *J. Phys. Chem. B*, **105**, 1422 (2001).

43. S. Wu, H. Han, Q. Tai, J. Zhang, S. Xu, C. Zhou, Y. Yang, H. Hu, B. Chen and X.-Z. Zhao, *J. Power Sources*, **182** 119 (2008).

44. T. W. Hamann, O. K. Farha and J. T. Hupp, *J. Phys. Chem. C*, **112**, 19756 (2008).

45. C. Lin, F.-Yu Tsai, M.-H. Lee, C.-H. Lee, Ta-C. Tien, L.-P. Wang and S.-Y. Tsai, *J. Mater. Chem.*, **19**, 2999 (2009).

46. J. R. Durrant, S. A. Haque and E. Palomares, *Coordin. Chem. Rev.*, **248**, 1247 (2004).

47. E. Palomares, J. N. Clifford, S. A. Haque, T. Lutz and J. R. Durrant, *J. Am. Chem. Soc.*, **125**, 475 (2003).

48. A. Zaban, S. G. Chen, S. Chappel and B. A. Gregg, *Chem. Commun.*, 2231 (2000).

49. N. G. Park, M. G. Kang, K. M. Kim, K. S. Ryu and S. H. Chang, *Langmuir*, **20**, 4246 (2004).

50. K. E. Kim, S. R. Jang, J. Park, R. Vittal and K. J. Kim, *Sol. Energy Mater. Sol. Cells*, **91**, 366 (2007).

51. Z. S. Wang, M. Yanagida, K. Sayama and H. Sugihara, *Chem. Mater.*, **18**, 2912 (2006).

52. S. Lee, J. Y. Kim, K. S. Hong, H. S. Jung, J. K. Lee and H. Shin, *Sol. Energy Mater. Sol. Cells*, **90**, 2405 (2006).

53. L. Zhang, Y. Shi, S. Peng, J. Liang, Z. Tao and J. Chen, *J. Photochem. Photobiol. A: Chem.*, **197**, 260 (2008).

54. J. Y. Kim, S. Lee, J. H. Noh, H. S. Jung and K. S. Hong, *J. Electroceram.*, **23**, 422 (2009).

55. K. Grigoras, S. Franssila and V.-M. Airaksinen, *Thin Solid Films*, **516**, 5551 (2008).

56. G. R. R. A. Kumara, K. Tennakone, V. P. S. Perera, A. Konno, S. Kaneko and M. Okuya, *J. Phys. D: Appl. Phys.*, **34**, 868 (2001).

57. V. Ganapathy, B. Karunagaran and S. Rhee, *J. Power Sources*, **195**, 5138 (2010).

58. J.-H. Yum, S.-R. Jang, P. Walter, T. Geiger, F. Nüesch, S. Kim, J. Ko, M. Grätzel and Md. K. Nazeeruddin, *Chem. Commun.*, 4680 (2007).

59. Z. Zhang, N. Evans, S. M. Zakeeruddin, R. Humphry-Baker and M. Grätzel, *J. Phys. Chem. C*, **111**, 398 (2007).

60. P. Wang, S. M. Zakeeruddin, P. Comte, R. Charvet, R. Humphry-Baker and M. Grätzel, *J. Phys. Chem. B*, **107**, 14336 (2003).

61. S. Ito, P. Liska, P. Comte, R. Charvet, P. Pechy, U. Bach, L. Schmidt-Mende, S. M. Zakeeruddin, A. Kay, Md. K. Nazeeruddin and M. Grätzel, *Chem. Commun.*, 4351 (2005).

62. A. Zaban, S. G. Chen, S. Chappel and B. A. Gregg, *Chem. Commun.*, 2231 (2000).

63. Z. Zhang, S. M. Zakeeruddin, B. C. O'Regan, R. Humphry-Baker and M. Grätzel, *J. Phys. Chem. B*, **109**, 21818 (2005).

64. N. R. Neale, N. Kopidakis, J. van de Lagemaat, M. Grätzel and A. J. Frank, *J. Phys. Chem. B*, **109**, 23183 (2005).

65. J. Lim, Y. S. Kwon and T. Park, *Chem. Commun.*, **47**, 4147 (2011).

66. M. Grätzel, *J. Photochem. Photobiol. C*, **4**, 145 (2003).

67. H. Lindström, A. Holmberg, E. Magnusson, S.-E. Lindquist, L. Malmqvist and A. Hagfeldt, *Nano Lett.*, **1**, 97 (2001).

68. H. Seo, M.-K. Son, I. Shin, J.-K. Kim, K.-J. Lee, K. Prabakar and H.-J. Kim, *Electrochim. Acta*, **55**, 4120 (2010).

69. M. K. Nazeeruddin, F. D. Angelis, S. Fantacci, A. Selloni, G. Viscardi, P. Liska, S. Ito, B. Takeru and M. Grätzel, *J. Am. Chem. Soc.*, **127**, 16835 (2005).

70. F. Hirose, M. Shikaku, Y. Kimura and M. Niwano, *J. Electrochem. Soc.*, **157**, B1578 (2010).

71. S.-H. Lim and S.-W. Rhee, *RSC Adances*, in press (2011).

72. W.-T. Chuang, B.-S. Chen, K.-Y. Chen, C.-C. Hsieh and P.-T. Chou, *Chem. Commun.*, 6982 (2009).

73. Y. Kim, B. J. Yoo, R. Vittal, Y. Lee, N.-G. Park and K.-J. Kim, *J. Power Sources*, **175**, 814 (2008).

74. S. Y. Huang, G. Schlichthörl, A. J. Nozik, M. Grätzel and A. J. Frank, *J. Phys. Chem. B*, **101**, 2576 (1997).

75. Y. Liu, A. Hagfeldt, X.-R. Xiao and S.-E. Lindquist, *Sol. Energy Mater. Sol. Cells*, **55**, 267 (1998).

76. G. Schlichthörl, S. Y. Huang, J. Sprague and A. J. Frank, *J. Phys. Chem. B*, **101**, 8319 (1997).

77. S. Nakade, T. Kanzaki, W. Kubo, T. Kitamura, Y. Wada and S. Yanagida, *J. Phys. Chem. B*, **109**, 3480 (2005).

78. N. Kopidakis, K. D. Benkstein, J. van de Lagemaat and A. J. Frank, *J. Phys. Chem. B*, **107**, 11307 (2003).

79. S. Pelet, J.-E. Moser and M. Grätzel, *J. Phys. Chem. B*, **104**, 1791 (2000).

80. B. Bhattacharya, J. Y. Lee, J. Geng, H.-T. Jung and J.-K. Park, *Langmuir*, **25**, 3276 (2009).

81. A. B. F. Martinson, T. W. Hamann, M. J. Pellin and J. T. Hupp, *Chem.-Eur. J.*, **14**, 4458 (2008).

82. P. R. F. Barnes, A. Y. Anderson, S. E. Koops, J. R. Durrant and B. C. O'Regan, *J. Phys. Chem. C*, **113**, 1126 (2009).

83. H. K. Dunn and L. M. Peter, *J. Phys. Chem. C*, **113**, 4726 (2009).

84. J. Bisquert, F. Fabregat-Santiago, I. Mora-Sero, G. Garcia-Belmonte and S. Gimenez, *J. Phys. Chem. C*, **113**, 17278 (2009).

85. N. Papageorgiou, M. Grätzel and P. P. Infelta, *Sol. Energy Mater. Sol. Cells*, **44**, 405 (1996).

86. N. Papageorgiou, C. Barbe and M. Grätzel, *J. Phys. Chem. B*, **102**, 4156 (1998).

87. C. Y. Chen, M. K. Wang, J. Y. Li, N. Poortrakulchote, L. Alibabaei, C. H. Ngoc-le, J. D. Decoppet, J. H. Tsai, C. Grätzel, C. G. Wu, S. M. Zakeeruddin and M. Grätzel, *ACS Nano*, **3**, 3103 (2009).

88. F. Cao, G. Oskam and P. C. Senadeera, *J. Phys. Chem.*, **99**, 17071 (1995).

89. W. Cubo, K. Murakoshi, T. Kitamura, S. Yoshida, M. Haruki, K. Hanabusa, H. Shirai, Y. Wada and S. Yanagida, *J. Phys. Chem. B*, **105**, 12809 (2001).

90. P. Wang, S. M. Zakeeruddin, J. E. Moser, M. K. Nazeeruddin, T. Sekiguchi and M. Grätzel, *Nat. Mater.*, **2**, 402 (2003).

91. L. Wang, S. Fang, Y. Lin, X. Zhou and M. Li, *Chem. Commun.*, 5687 (2005).

92. J. H. Wu, Z. Lan, J. M. Lin, M. L. Huang, S. C. Hao, T. Sato and S. Yin, *Adv. Mater.*, **19**, 4006 (2007).

93. J. Wu, S. Hao, Z. Lan, J. Lin, M. Huang, Y. Huang, L. Fang, S. Yin and T. Sato, *Adv. Mater.*, **17**, 2645 (2007).

94. J. Shi, S. Peng, J. Pei, Y. Liang, F. Cheng and J. Chen, *ACS Appl. Mater. Interfaces*, **1**, 944 (2009).

95. U. Bach, D. Lupo, P. Comte, J.-E. Moser, F. Weissörtel, J. Salbeck, H. Spreitzer and M. Grätzel, *Nature*, **395**, 583 (1998).

96. Y. Saito, N. Fukuri, R. Senadeera, T. Kitamura, Y. Wada and S. Yanagida, *Electrochem. Commun.*, **6**, 71 (2003).

97. J. Krüger, R. Plass, M. Grätzel, P. J. Cameron and L. M. Peter, *J. Phys. Chem. B*, **107**, 7536 (2003).

98. J. Xia, N. Masaki, M. L. Cantu, Y. Kim, K. Jiang and S. Yanagida, *J. Am. Chem. Soc.*, **130**, 1258 (2008).

99. B. O'Regan and D. T. Schwartz, *Chem. Mater.*, **10**, 1501 (1998).

100. B. O'Regan, F. Lenzmann, R. Muis and J. Wienke, *Chem. Mater.*, **14**, 5023 (2002).

101. H. J. Lee, P. Chen, S.-J. Moon, F. Sauvage, K. Sivula, T. Bessho, D. R. Gamelin, P. Comte, S. M. Zakeeruddin, S. I. Seok, M. Grätzel and M. K. Nazeeruddin, *Langmuir*, **25**, 7602 (2009).

102. P. Wang, S. M. Zakeeruddin, J.-E. Moser and M. Grätzel, *J. Phys. Chem. B*, **107**, 13280 (2003).

103. P. Wang, S. M . Zakeeruddin, J.-E. Moser, R. H. Baker and M. Grätzel, *J. Am. Chem. Soc.*, **126**, 7164 (2004).

104. D. Kuang, C. Klein, Z. Zhang, S. Ito, J.-E. Moser, S. M. Zakeeruddin and M. Grätzel, *Small*, **3**, 2094 (2007).

105. D. Kuang, P. Wang, S. Ito, S. M. Zakeeruddin and M. Grätzel, *J. Am. Chem. Soc.*, **128**, 7732 (2006).

106. Y. Bai, Y. Cao, J. Zhang, M. Wang, R. Li, P. Wang, S. M. Zakeeruddin and M. Grätzel, *Nat. Mat.*, **7**, 626 (2008).

107. W. Kubo, Y. Makimoto, T. Kitamura, Y. Wada and S. Yanagida, *Chem. Lett.*, 948 (2002).

108. S. Anandan, S. Pitchumani, B. Muthuraaman and P. Maruthamuthu, *Sol. Energy Mater. Sol. Cells*, **90**, 1715 (2006).

109. T. Stergiopoulos, I. M. Arabatzis, G. Katsaros and P. Falaras, *Nano Lett.*, **2**, 1259 (2002).

110. G. Katsaros, T. Stergiopoulos, I. M. Arabatzis, K. G. Papadokostaki and P. Falaras, *J. Photochem. Photobiol. A*, **149**, 191 (2002).

111. J. Wu, S. Hao, Z. Lan, J. Lin, M. Huang, Y. Huang, P. Li, S. Yin and T. Sato, *J. Am. Chem. Soc.*, **130**, 11568 (2008).

112. Y. Zhou, W. Xiang, S. Chen, S. Fang, W. Zhou, J. Zhang and Y. Lin, *Electrochim. Acta*, **54**, 6645 (2009).

113. W. Kwon and S.-W. Rhee, *J. Power Sources*, submitted (2011).

114. R. A. Jain, *Biomaterials*, **21**, 2475 (2000).

115. J. R. Jennings and L. M. Peter, *J. Phys. Chem. C*, **111**, 16100 (2007).

116. H. J. Snaith and M. Grätzel, *Adv. Mater.*, **19**, 3643 (2007).

117. H. J. Snaith, A. J. Moule, C. Klein, K. Meerholz, R. H. Friend and M. Grätzel, *Nano Lett.*, **7**, 3372 (2007).

118. L. Schmidt-Mende, S. M. Zakeeruddin and M. Grätzel, *Appl. Phys. Lett.*, **86**, 013504 (2005).

119. I.-K. Ding, N. Tetreault, J. Brillet, B. E. Hardin, E. H. Smith, S. J. Rosenthal, F. Sauvage, M. Grätzel and M. D. McGehee, *Adv. Funct. Mater.*, **19**, 1 (2009).

120. P. Wang, S. M. Zakeeruddin, R. Humphry-Baker and M. Grätzel, *Chem. Mater.*, **16**, 2694 (2004).

121. P. Wang, B. Wenger, R. Humphry-Baker, J.-E. Moser, J. Teuscher, W. Kantlehner, J. Mezger, E. V. Stoyanov, S. M. Zakeeruddin and M. Grätzel, *J. Am. Chem. Soc.*, **127**, 6850 (2005).

122. H. Han, U. Bach, Y. B. Cheng and R. A. Caruso, *Appl. Phys. Lett.*, **90**, 213510 (2007).

123. J. Zhang, H. Han, S. Wu, S. Xu, Y. Yang, C. Zhou and X. Zhao, *Solid State Ionics*, **178**, 1595 (2007).

124. X. Zhang, H. Yang, H. M. Xiong, F. Y. Li and Y. Y. Xia, *J. Power Sources*, **160**, 1541 (2006).

125. G. Nazmutdinova, S. Sensfuss, M. Schr€odner, A. Hinsch, R. Sastrawan, D. Gerhard, S. Himmler and P. Wasserscheid, *Solid State Ionics*, **177**, 3141 (2006).

126. B. I. Ito, J. N. de Freitas, M. A. De Paoli and A. F. Nogueira, *J. Braz. Chem. Soc.*, **19**, 688 (2008).

127. E. Olsen, G. Hagen and S.-E. Lindquist, *Sol. Energy Mater. Sol. Cells*, **63**, 267 (2000).

128. Z. Zhang, P. Chen, T. N. Murakami, S. M. Zakeeruddin and M. Grätzel, *Adv. Funct. Mater.*, **18**, 341 (2008).

129. M. Wang, N. Chamberland, L. Breau, J.-E. Moser, R. Humphry-Baker, B. Marsan, S. M. Zakeeruddin and M. Grätzel, *Nat. Chem.*, **2**, 385 (2010).

130. G. Oskam, B. Bergeron, G. J. Meyer and P. C. Searson, *J. Phys. Chem. B*, **105**, 6867 (2001).

131. H. Nusbaumer, J.-E. Moser, S. M. Zakeeruddin, M. K. Nazeerud-

din and M. Grätzel, *J. Phys. Chem. B*, **105**, 10461 (2001).

132. S. Hattori, Y. Wada, S. Yanagida and S. Fukuzumi, *J. Am. Chem. Soc.*, **127**, 9648 (2005).

133. J. Ferber, R. Stangl and J. Luther, *Sol. Energy Mater. Sol. Cells*, **53**, 29 (1998).

134. A. Hagfeldt, B. Didriksson, T. Palmqvist, H. Lindstrom, S. Sodergren, H. Rensmo and S. E. Lindquist, *Sol. Energy Mater. Sol. Cells*, **31**, 481 (1994).

135. N. Papageorgiou, W. F. Maier and M. Grätzel, *J. Electrochem. Soc.*, **144**, 876 (1997).

136. G. Wang, R. Lin, Y. Lin, X. Li, X. Zhou and X. Xiao, *Electrochem. Acta*, **50**, 5546 (2005).

137. S. Hao, J. Wu, J. Lin and Y. Huang, *Compos. Interfaces*, **13**, 899 (2006).

138. N. Papageorgiou, *Coord. Chem. Rev.*, **248**, 1421 (2004).

139. A. Hauch and A. Georg, *Electrochim. Acta*, **46**, 3457 (2001).

140. X. Fang, T. Ma, G. Guan, M. Akiyama, T. Kida and E. Ade, *J. Electroanal. Chem.*, **570**, 257 (2004).

141. C. M. Chen, C. H. Chen and T. C. Wei, *Electrochem. Acta*, **55**, 1687 (2010).

142. S. S. Kim, Y. C. Nah, Y. Y. Noh, J. Jo and D. Y. Kim, *Electrochim. Acta*, **51**, 3814 (2006).

143. P. Li, J. Wu, J. Lin, M. Huang, Z. Lan and Q. Li, *Electrochim. Acta*, **53**, 4161 (2008).

144. C. H. Yoon, R. Vittal, J. Lee, W. S. Chae and K. J. Kim, *Electrochim. Acta*, **53**, 2890 (2008).

145. A. M. K. Dagamseh, B. Vet, F. D. Tichelaar, P. Sutta and M. Zeman, *Thin Solid Films*, **516**, 7844 (2008).

146. X. Fang. T. Ma, M. Akiyama, G. Guan, S. Tsunematsum and E. Abe, *Thin Solid Films*, **472**, 242 (2005).

147. M. Toivola, J. Halme, K. Miettunen, K. Aitola and P. D. Lund, *Int. J. Energy Res.*, **33**, 1145 (2009).

148. G. Smestad, G. Bignozzi and R. Argazzi, *Sol. Energy Mater. Sol. Cells*, **32**, 259 (1994).

149. M. Grätzel, *Nature*, **414**, 338 (2001).

150. G. Calogero, F. Bonaccorso, O. M. Marago, P. G. Gucciardim and G. D. Marco, *Dalton Trans.*, **39**, 2903 (2010).

151. X. Fan, Z. Chu, F. Wang, C. Zhang, L. Chen, Y. Tang and D. Zou, *Adv. Mater.*, **20**, 592 (2008).

152. K. Okada, H. Matsui, T. Kawashima, T. Ezure and N. Tanabe, *J. Photochem. Photobiol. A*, **164**, 193 (2004).

153. Y. Chiba, A. Islam, Y. Watanabe, R. Komiya, N. Koide and L. Han, *Jpn. J. Appl. Phys.*, **45**, L638 (2006).

154. G. Q. Wang, R. F. Lin, M. Wang, C. N. Zhang, Y. Lin, X. R. Xiao and X. P. Li, *Chin. Chem. Lett.*, **15**, 1369 (2004).

155. X. Mathew, G. W. Thompson, V. P. Singh, J. C. McClure, S. Velumani, N. R. Mathews and P. J. Sebastian, *Sol. Energy Mater; Sol. Cells*, **76**, 293 (2003).

156. T. Ma, X. Fang, M. Akiyama, K. Inoue, H. Noma and E. Abe, *J. Electroanal. Chem.*, **574**, 77 (2004).

157. M. Toivola, F. Ahlskog and P. Lund, *Sol. Energy Mater. Sol. Cells*, **90**, 2881 (2006).

158. K. Suzuki, M. Yamaguchi, M. Kumagai and S. Yanagida, *Chem. Lett.*, **32**, 28 (2003).

159. E. Ramasamy, W. J. Lee, D. Y. Lee and J. S. Song, *Electrochem.*

Commun., **10**, 1087 (2008).

160. K. Imoto, K. Takahashi, T. Yamaguchi, T. Komura, J. Nakamura and K. Murata, *Sol. Energy Mater. Sol. Cells*, **79**, 459 (2003).

161. E. Ramasamy, J. W. Lee, D. Y. Lee and J. S. Song, *Appl. Phys. Lett.*, **90**, 173103 (2007).

162. E. Ramasamy, J. Chun and J. W. Lee, *Carbon*, **48**, 4556 (2010).

163. Y. Saito, T. Kitamura, Y. Wada and S. Yanagida, *Chem. Lett.*, **31**, 1060 (2002).

164. J. B. Xia, N. Masaki, K. J. Jiang and S. Yanagida, *J. Mater. Chem.*, **17**, 2845 (2007).

165. Z. Huang, X. Liu, K. Li, D. Li, Y. Luo, H. Li, W. Song, L. Chen and Q. Meng, *Electrochem. Commun.*, **9**, 596 (2007).

166. T. N. Murakami, S. Ito, Q. Wang, Md. K. Nazeeruddin, T. Bessho, I. Cesar, P. Liska, R. H. Baker, P. Comte, P. Péchy and Michael Grätzelz, *J. Electrochem. Soc.*, **153**, A2255 (2006).

167. P. Joshi, L. Zhang, Q. Chen, D. Galipeau, H. Fong and Q. Qiao, *ACS Appl. Mater. Inter.*, **2**, 3572 (2010).

168. Z. Huang, X. Liu, K. Li, D. Li, Y. Luo, H. Li, W. Song, Li. Chen and Q. Meng, *Electrochem. Commun.*, **9**, 596 (2007).

169. E. Ramasamy, W. J. Lee, D. Y. Lee and J. S. Song, *Electrochem. Commun.*, **10**, 1087 (2008).

170. C. E. Banks, T. J. Davies, G. G. Wildgoose and R. G. Compton, *Chem. Commun.*, **7**, 829 (2005).

171. G. Wang, W. Xing and S. Zhuo, *J. Power Sources*, **194**, 568 (2009).

172. S. Peng, F. Cheng, J. Shi, J. Liang, Z. Tao and J. Chen, *Sol. State Sci.*, **11**, 2051 (2009).

173. G. Veerappan, K. Bojan and S.-W. Rhee, *ACS Appl. Mater. Inter.*, **3**, 857 (2011).

174. B. Fang, S. Q. Fan, J. H. Kim, M. S. Kim, M. W. Kim, N. K. Chaudhari, J. J. Ko and J. S. Yu, *Langmuir*, **26**, 11238 (2010).

175. S. Q. Fan, B. Fang, J. H. Kim, B. S. Jeong, C. W. Kim, J. S. Yu and J. J. Ko, *Langmuir*, **26**, 13644 (2010).

176. E. Ramasamy and J. W. Lee, *Carbon*, **48**, 3715 (2010).

177. D.-J. Yun, K.-P. Hong, S.-H. Kim, W.-M. Yun, J.-Y. Jang, W.-S. Kwon, C.-E. Park and S.-W. Rhee, *ACS Appl. Mater. Inter.*, **3**, 857 (2011).

178. D.-J. Yun and S.-W. Rhee, *J. Mater. Chem.*, submitted (2011).

Shi-Woo Rhee is currently a Professor and Director of the System on Chip Process Research Center, Pohang University of Science and Technology (POSTECH), Pohang, Korea (1986~present). He received his B.S. (1974) from Seoul National University and M.S. (1976) from Korea Advanced Institute of Science and Technology (KAIST) and Ph. D (1984) from Massachusetts Institute of Technology (MIT), U.S.A. in Chemical Engineering. He worked as a researcher in the Korea Institute of Science and Technology (KIST) (1976-79) and as a post-doctoral researcher in the Department of Materials Science and Engineering at MIT (1984-86). He has been working on the materials and processes for semiconductor devices and solar cells.